ChemComm

COMMUNICATION

View Article Online
View Journal | View Issue

Cite this: *Chem. Commun.*, 2025, **61**, 141

Received 11th October 2024,
Accepted 25th November 2024

DOI: 10.1039/d4cc05385k

rsc.li/chemcomm

An Fe-doped Ni-based oxalate framework with a favorable electronic structure for electrocatalytic water and urea oxidation†

Chunzi Yang,[ac] Ming Zhao,[a] Chunmei Zhang,[a] Shan Zhang,*[a] Dongdong Zhu *[b] and Chunxian Guo *[a]

An Fe-doped Ni-based oxalate framework, synthesized *via* a facile co-precipitation method, is applied as an excellent bi-functional electrocatalyst for water and urea oxidation reactions. The obtained framework achieved a large current density of 100 mA cm^{-2} at 1.497 V and 1.375 V (*vs.* RHE) for the OER and UOR, highlighting its potential for practical hydrogen production.

The increasing energy demand and environmental issues call for clean energy carriers. Hydrogen attracts much interest due to its high energy density (142 MJ kg^{-1}) and zero carbon dioxide emission.[1] Electrocatalytic water splitting is recognized as a promising route to produce green hydrogen. Traditional water splitting involves the cathodic hydrogen evolution reaction (HER) and anodic oxygen evolution reaction (OER). Since the OER is a sluggish four-electron-transfer process,[2] high potentials much more positive than the theoretical potential (1.23 V *vs.* RHE) are always required. Therefore, developing highly efficient OER electrocatalysts is essential for practical application of water electrolysis. Despite great achievements having been made in the design of advanced OER electrocatalysts, the energy consumption at the anode of water electrolysis is still large. Fortunately, the anodic OER can be replaced by some other oxidation reactions, which are thermodynamically more favourable.[3,4] Among them, the urea oxidation reaction (UOR) receives great attention because of its low thermodynamic potential of only 0.37 V *vs.* RHE. Moreover, urea can be decomposed into non-toxic N_2, O_2 and H_2O products *via* the UOR, which provides an environmentally friendly way to treat urea-containing industrial and sanitary wastewater. Coupling the more favored anodic UOR with the cathodic HER, a urea-assisted water electrolyzer enables energy-saving hydrogen production and wastewater treatment, simultaneously.[5] However, the UOR still suffers from an intrinsically sluggish six-electron-transfer process, and highly active electrocatalysts for the UOR are always required. In this regard, it is urgent to construct highly active and robust bi-functional electrocatalysts for the OER and UOR to achieve efficient and stable hydrogen generation.[6]

Some noble metal-based materials are demonstrated as advanced electrocatalysts for the OER/UOR.[7,8] However, the extraordinarily high price and low abundance of these noble metals severely limit their further application, thus making transition metal-based materials promising alternatives. Despite various transition metal-based materials having been reported for the OER,[9,10] only Ni-based materials emerge as up-to-date active and most widely explored UOR electrocatalysts.[11–14] The pre-oxidized NiOOH with Ni^{3+} species is identified as the real active species for catalyzing urea oxidation.[15–19] Such *in situ* electrochemical surface reconstruction from Ni^{2+} to highly active Ni^{3+} species plays a crucial role in determining the UOR activity. To promote the formation of high-valence Ni^{3+} sites, heteroatom doping is reported as an effective strategy, as doped heteroatoms can modify the electronic structure of Ni cations.[20] For instance, Fe doping can facilitate the generation of Ni^{3+} species, contributing to dramatically enhanced OER activity,[21–23] though the exact mechanism of Fe doping is still under debate.[24–26] It is also believed that Fe incorporation into NiOOH leads to improved electrical conductivity, which is highly desirable for electrochemical processes.[27]

Organic ligands with negative functional groups such as benzene dicarboxylic (BDC) are introduced to produce metal–organic frameworks (MOFs) as highly efficient UOR/OER electrocatalysts.[28] Similarly, oxalate is also strongly electrophilic due to its two COO^- groups.[29,30] Taking advantage of the electro-withdrawing property, constructing oxalate-based catalysts can achieve a high percentage of active Ni^{3+} species, and

[a] School of Materials Science and Engineering, Suzhou University of Science and Technology, Suzhou 215009, China. E-mail: cxguo@usts.edu.cn, zs@usts.edu.cn
[b] School of Chemistry and Materials Science, Institute of Advanced Materials and Flexible Electronics (IAMFE), Nanjing University of Information Science and Technology, Nanjing 210044, China. E-mail: dd.zhu@nuist.edu.cn
[c] School of Environmental Science and Engineering, Suzhou University of Science and Technology, Suzhou 215009, China

† Electronic supplementary information (ESI) available. See DOI: https://doi.org/10.1039/d4cc05385k

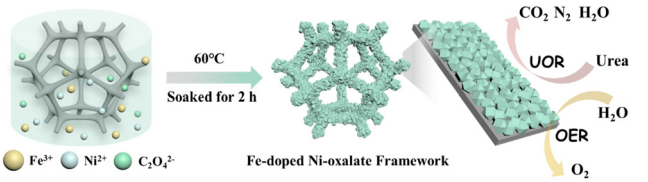

Scheme 1 Schematic illustration of the synthetic route for $Ni_xFe_{2-x}C_2O_4$.

improved OER/UOR performance can be expected.[11] However, reports on oxalate-related materials as bi-functional OER and UOR electrocatalysts are still very limited. Taken together, it is proposed to combine Fe doping and using oxalate ligands in catalyst design to facilitate the generation of Ni^{3+} species, thus boosting the OER and UOR performance. Additionally, the typical solvothermal method to prepare MOFs with a BDC ligand often requires organic solvents such as triethylamine and *N*,*N*-dimethylformamide,[31] and it is highly desirable to develop a facile and green strategy to obtain oxalate-based materials.

Herein, we report a series of Fe-doped Ni-based oxalate frameworks ($Ni_xFe_{2-x}C_2O_4$) with different ratios of Ni and Fe on nickel foam (NF) *via* a facile co-precipitation method (Scheme 1). Benefiting from the increased number of Ni^{3+} active sites caused by Fe doping and the oxalate ligand, the optimized $Ni_{0.6}Fe_{1.4}C_2O_4$ possesses superior catalytic activity towards the OER and UOR with small overpotentials and Tafel slopes. This work provides a low-cost and efficient bi-functional electrocatalyst for the OER and UOR.

XRD patterns of all $Ni_xFe_{2-x}C_2O_4$ samples (Fig. S1, ESI†) display similar diffraction peaks to those of $Ni_{0.6}Fe_{1.4}C_2O_4$ (Fig. 1a), which match well with $NiC_2O_4{\cdot}2H_2O$ (JPCDS No. 25-0581) and α-$FeC_2O_4{\cdot}2H_2O$ (JPCDS No. 23-0293). These results indicate the successful formation of Fe-doped Ni-oxalate, accompanying the color change of NF from metallic silver to greyish green (Fig. S2, ESI†). There is no noticeable disparity between diffraction peaks of Ni/Fe oxalates owing to the similar structure of Ni and Fe. The scanning electron microscopy (SEM) image of $Ni_{0.6}Fe_{1.4}C_2O_4$ in Fig. 1b shows that irregular nanocubes with a size of about 500 nm are stacked on the NF surface homogeneously. Compared to monometallic NiC_2O_4 and FeC_2O_4 samples (Fig. S3, ESI†), the deposition of $Ni_{0.6}Fe_{1.4}C_2O_4$ on NF is more compact and uniform. The transmission electron microscopy (TEM) image (Fig. 1c) reveals that the obtained irregular nanocubes are built by some nanoparticles. Furthermore, obvious lattice fringes of these nanoparticles can be clearly seen in high-resolution TEM images (Fig. 1d and Fig. S4, ESI†). The lattice spacing of 0.223 nm (inset in Fig. 1d) is well indexed to the (−314) plane of $NiC_2O_4{\cdot}2H_2O$ (JPCDS No. 25-0581). The Ni, Fe, C and O elements are evenly distributed across the whole irregular nanocubes (Fig. 1e), implying the homogeneous incorporation of Fe in $Ni_{0.6}Fe_{1.4}C_2O_4$. All the results above demonstrate the successful preparation of the Ni–Fe-oxalate framework on NF.

The surface composition and elemental valence state of $Ni_{0.6}Fe_{1.4}C_2O_4$ were determined by X-ray photoelectron spectroscopy (XPS). The high-resolution Ni 2p spectrum of $Ni_{0.6}Fe_{1.4}C_2O_4$ exhibits two different pairs of peaks (Fig. 2a), among which the peaks at 855.4 eV and 873.2 eV are attributed to $2p_{3/2}$ and $2p_{1/2}$ of Ni^{2+}, respectively. While the other pair of peaks at 857.5 eV and 876.5 eV are assigned to Ni^{3+} $2p_{3/2}$ and $2p_{1/2}$, respectively.[15] Moreover, the corresponding satellite peaks are observed at 861.1 eV and 880 eV.[32] A small peak of 852.4 eV representing metallic Ni comes from the NF substrate.[30,33] It is worth noting that the binding energy of Ni 2p in $Ni_{0.6}Fe_{1.4}C_2O_4$ has a positive shift of 0.36 eV compared to that of NiC_2O_4, indicating electron redistribution around Ni sites upon Fe doping. The content of active Ni^{3+} species in $Ni_{0.6}Fe_{1.4}C_2O_4$ is calculated to be 24.62%, while this value for NiC_2O_4 is only 7.99%, giving strong evidence that Fe doping increases the Ni^{3+} content in $Ni_{0.6}Fe_{1.4}C_2O_4$. Fig. 2b displays the Fe 2p spectra of the $Ni_{0.6}Fe_{1.4}C_2O_4$ and FeC_2O_4 samples. For $Ni_{0.6}Fe_{1.4}C_2O_4$, there are two peaks at around 712.16 eV and 724.34 eV, which belong to Fe^{2+} $2p_{3/2}$ and $2p_{1/2}$, respectively.[34] Compared with the Fe 2p spectrum of FeC_2O_4, negative displacement of 0.4 eV

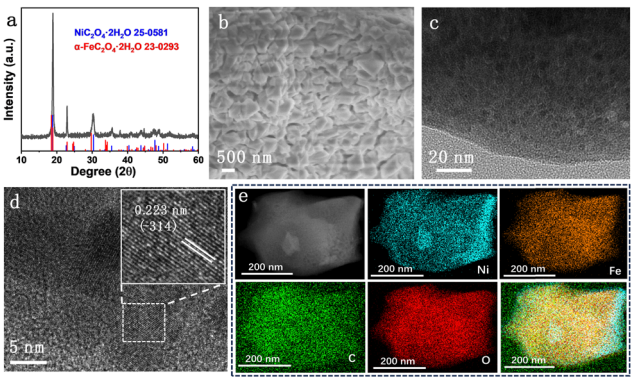

Fig. 1 (a) XRD pattern of $Ni_{0.6}Fe_{1.4}C_2O_4$, (b) SEM, (c) TEM and (d) HRTEM images of $Ni_{0.6}Fe_{1.4}C_2O_4$, and (e) the corresponding EDX elemental mapping of Ni, Fe, C and O of $Ni_{0.6}Fe_{1.4}C_2O_4$.

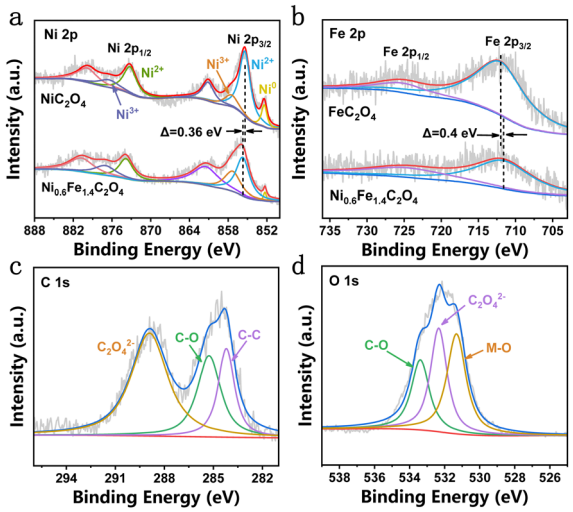

Fig. 2 High-resolution XPS spectra of (a) Ni 2p of NiC_2O_4 and $Ni_{0.6}Fe_{1.4}C_2O_4$, (b) Fe 2p of FeC_2O_4 and $Ni_{0.6}Fe_{1.4}C_2O_4$, and (c) C 1s and (d) O 1s of $Ni_{0.6}Fe_{1.4}C_2O_4$.

for $Ni_{0.6}Fe_{1.4}C_2O_4$ can be observed. Considering the aforementioned binding energy change of Ni, it is suggested that electrons transfer from Ni to Fe, resulting in charge-redistribution around the active metal sites. Three peaks can be obtained in the C 1s spectrum (Fig. 2c), where 284.2 eV and 285.3 eV can be assigned to C–C and C–O bonds, respectively, while 288.9 eV corresponds to $C_2O_4^{2-}$.[34] For the O 1s spectrum, as shown in Fig. 2d, three peaks can be obtained. The peaks at 531.3 eV and 533.4 eV can be well indexed to the metal–O (M–O) bond and C–O bond, respectively, while the peak located at 532.3 eV is ascribed to $C_2O_4^{2-}$, which is consistent with a previous report.[30]

Thanks to the generation of desirable Ni^{3+} active sites, $Ni_{0.6}Fe_{1.4}C_2O_4$ can be utilized as a bi-functional electrocatalyst for both the OER and UOR. As can be seen from Fig. 3a, $Ni_{0.6}Fe_{1.4}C_2O_4$ shows excellent OER performance, surpassing other electrocatalysts with various compositions. The overpotentials of $Ni_xFe_{2-x}C_2O_4$ at the current density of 10 mA cm^{-2} (η_{10}) and 100 mA cm^{-2} (η_{100}) are collected in Fig. S5a (ESI†) for comparison. Of note, η_{10} is obtained from CV to avoid the influence of the pre-oxidation peak (Fig. S5b, ESI†). $Ni_{0.6}Fe_{1.4}C_2O_4$ displays the smallest η_{100} of 267 mV. In contrast, the single component NiC_2O_4 needs a large η_{100} of 461 mV. Such results indicate that Fe incorporation plays a pivotal role in boosting the OER performance. The superior OER activity of $Ni_{0.6}Fe_{1.4}C_2O_4$ is also demonstrated by a small Tafel slope of 22.63 mV dec^{-1} (Fig. 3b), implying its fast OER kinetics. The excellent OER performance of $Ni_{0.6}Fe_{1.4}C_2O_4$ makes it among the best-performing OER electrocatalysts (Table S1, ESI†). To further reveal the origin of the high OER activity of $Ni_{0.6}Fe_{1.4}C_2O_4$, the electrochemically active surface area (ECSA) and electrochemical impedance spectroscopy (EIS) were employed. As seen from Fig. S6 (ESI†), $Ni_{0.6}Fe_{1.4}C_2O_4$ possesses the largest C_{dl} of 10.7 mF cm^{-2}, implying its largest ECSA with more active sites exposed. The intrinsic activity is further compared (Fig. S7a, ESI†), among which $Ni_{0.6}Fe_{1.4}C_2O_4$ displays the highest intrinsic OER activity. Moreover, the smallest charge transfer resistance of $Ni_{0.6}Fe_{1.4}C_2O_4$ in the Nyquist plots (Fig. S7b and inset, ESI†) suggests low charge transfer resistance at the electrode/electrolyte interface. As shown in the Bode diagrams (Fig. S8, ESI†), the peak of $Ni_{0.6}Fe_{1.4}C_2O_4$ disappears in the high frequency region at a voltage of 1.30 V, indicating that surface Ni^{2+} is completely reconstructed into a higher valence state, which is the actual active site for the OER process.[35] The voltage of $Ni_{0.6}Fe_{1.4}C_2O_4$ is much lower than that of NiC_2O_4, implying that Fe incorporation benefits the formation of active NiOOH species. Chronoamperometric measurement of $Ni_{0.6}Fe_{1.4}C_2O_4$ is conducted to examine its OER durability. The current density displayed some loss during 50-h electrocatalysis, implying its moderate stability performance (Fig. 3c). Such substandard stability results may be attributed to its structural change during the OER process. To uncover the possible catalyst evolution, the morphology, composition and structure of $Ni_{0.6}Fe_{1.4}C_2O_4$ after the stability test were characterized. The nanocube morphology of $Ni_{0.6}Fe_{1.4}C_2O_4$ can still be observed, while some nanosheets also generate on the surface of the nanocubes (Fig. S9a and b, ESI†). Importantly, $Ni(OH)_2$ species emerge as catalytically active sites for the OER (Fig. S9 and S10, ESI†).

Besides the OER, the as-prepared $Ni_{0.6}Fe_{1.4}C_2O_4$ is also performed for the UOR. Impressively, $Ni_{0.6}Fe_{1.4}C_2O_4$ displays greatly improved current densities when 0.33 M urea is added in 1.0 M KOH electrolyte (Fig. S11a, ESI†), and the potential to afford the UOR current density of 10 mA cm^{-2} is 1.36 V *vs.* RHE (Fig. 3d). The corresponding smallest Tafel slope of 15.12 mV dec^{-1} for $Ni_{0.6}Fe_{1.4}C_2O_4$ further implies its fast UOR kinetics (Fig. 3e). Furthermore, considering the overpotentials required at current densities of 10 and 100 mA cm^{-2} (Fig. S11b, ESI†), $Ni_xFe_{2-x}C_2O_4$ is most active towards the UOR. Specifically, $Ni_{0.6}Fe_{1.4}C_2O_4$ requires a potential of 1.375 V *vs.* RHE to reach 100 mA cm^{-2}, while NiC_2O_4 and FeC_2O_4 require more positive potentials of 1.452 V and 1.418 V *vs.* RHE, respectively. For $Ni_{0.6}Fe_{1.4}C_2O_4$, both large ECSA with more exposed active sites, and higher intrinsic activity contribute to its excellent UOR performance (Fig. S12 and S13, ESI†). The smallest charge transfer resistance (Fig. S14, ESI†) of $Ni_{0.6}Fe_{1.4}C_2O_4$ further suggests the fast charge transfer at the electrode/electrolyte interface. As displayed in Table S2 (ESI†), $Ni_{0.6}Fe_{1.4}C_2O_4$ is one of the most efficient UOR electrocatalysts among these recently reported results. Bode diagrams (Fig. S15, ESI†) show that the peak of $Ni_{0.6}Fe_{1.4}C_2O_4$ in the high frequency region disappears at the voltage of 1.38 V, meaning that active NiOOH species are generated, which is earlier than that of NiC_2O_4 and FeC_2O_4. Moreover, $Ni_{0.6}Fe_{1.4}C_2O_4$ exhibits the smallest phase angle for the UOR, which reflects rapid dissociation kinetics of urea and strong electrooxidation ability of the reaction intermediates. Afterwards, chronoamperometric measurement of $Ni_{0.6}Fe_{1.4}C_2O_4$ was carried out in 1.0 M KOH and 0.33 M urea with refreshing the electrolyte three times (Fig. 3f). No obvious attenuation is observed over a continuous 40-h test, validating the excellent durability of $Ni_{0.6}Fe_{1.4}C_2O_4$ for the UOR. Post-characterization was conducted to investigate the morphology and structure change of $Ni_{0.6}Fe_{1.4}C_2O_4$. After the UOR stability test, the nanocube morphology of $Ni_{0.6}Fe_{1.4}C_2O_4$ is well

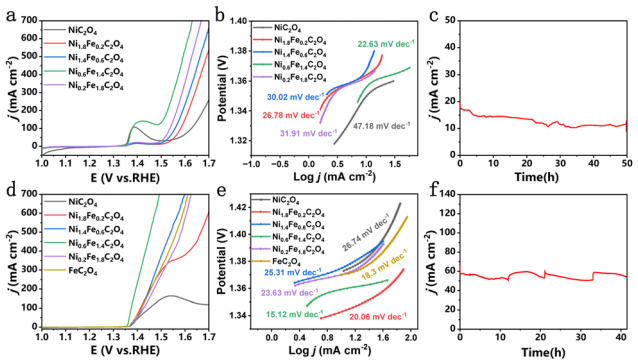

Fig. 3 (a) LSV curves of $Ni_xFe_{2-x}C_2O_4$ for the OER in 1.0 M KOH, (b) the corresponding Tafel slopes, and (c) stability test of $Ni_{0.6}Fe_{1.4}C_2O_4$ for the OER. (d) LSV curves of $Ni_xFe_{2-x}C_2O_4$ for the UOR in 1.0 M KOH and 0.33 M urea, (e) the corresponding Tafel slopes, and (f) stability test of $Ni_{0.6}Fe_{1.4}C_2O_4$ for the UOR.

retained, while some nanosheets can be observed on the surface of the nanocubes (Fig. S16a and b, ESI†). Similarly, $Ni(OH)_2$ generates as real active species for the UOR (Fig. S16c and S17, ESI†). Though the original $Ni_{0.6}Fe_{1.4}C_2O_4$ is transferred to Fe-doped $Ni(OH)_2$ during long-term electrolysis, Ni and Fe elements are still evenly distributed throughout the whole sample (Fig. S16d, ESI†).

In summary, an Fe doped Ni-based oxalate framework is facilely prepared through a one-step co-precipitation method, which is applied as a bi-functional electrocatalyst for the OER and UOR. Both Fe incorporation and introduction of electrophilic oxalate ligands facilitate the formation of highly desirable Ni^{3+} species. Therefore, the as-prepared $Ni_{0.6}Fe_{1.4}C_2O_4$ exhibits excellent performance towards the OER and UOR. Potentials of 1.497 V and 1.375 V *vs.* RHE are required to afford a large current density of 100 mA cm^{-2} for the OER and UOR, respectively. This work provides a dual-modulation strategy to construct Ni^{3+} rich electrocatalysts, which are promising for a variety of oxidation reactions beyond the OER and UOR.

The authors are grateful to the National Natural Science Foundation of China (22302140, 22372113), the Natural Science Foundation of Jiangsu Province (BK20220641), and the National Key Research and Development Program of China (No. 2021YFA0910403).

Data availability

The data supporting this article have been included as part of the ESI.†

Conflicts of interest

There are no conflicts to declare.

Notes and references

1 T. Wang, X. Cao and L. Jiao, *eScience*, 2021, **1**, 69–74.
2 B. Deng, G. Yu, W. Zhao, Y. Long, C. Yang, P. Du, X. He, Z. Zhang, K. Huang, X. Li and H. Wu, *Energy Environ. Sci.*, 2023, **16**, 5210–5219.
3 Y. Sun, J. Wang, Y. Qi, W. Li and C. Wang, *Adv. Sci.*, 2022, **9**, e2200957.
4 Y. Zhu, X. Zhu, L. Bu, Q. Shao, Y. Li, Z. Hu, C.-T. Chen, C.-W. Pao, S. Yang and X. Huang, *Adv. Funct. Mater.*, 2020, **30**, 2004310.
5 Y. Diao, Y. Liu, G. Hu, Y. Zhao, Y. Qian, H. Wang, Y. Shi and Z. Li, *Biosens. Bioelectron.*, 2022, **211**, 114380.
6 X. Jia, H. Kang, X. Yang, Y. Li, K. Cui, X. Wu, W. Qin and G. Wu, *Appl. Catal., B*, 2022, **312**, 121389.
7 T. Kwon, H. Yang, M. Jun, T. Kim, J. Joo, J. Kim, H. Baik, J. Y. Kim and K. Lee, *J. Mater. Chem. A*, 2021, **9**, 14352–14362.
8 M. Zhong, M. Xu, S. Ren, W. Li, C. Wang, M. Gao and X. Lu, *Energy Environ. Sci.*, 2024, **17**, 1984–1996.
9 X. Zhang, A. Wu, D. Wang, Y. Jiao, H. Yan, C. Jin, Y. Xie and C. Tian, *Appl. Catal., B*, 2023, **328**, 122474.
10 C. Chen, M. Sun, F. Zhang, H. Li, M. Sun, P. Fang, T. Song, W. Chen, J. Dong, B. Rosen, P. Chen, B. Huang and Y. Li, *Energy Environ. Sci.*, 2023, **4**, 1685–1696.
11 J. Kim, M. C. Kim, S. S. Han and K. Cho, *Adv. Funct. Mater.*, 2024, **34**, 2315625.
12 P. Wang, X. Bai, H. Jin, X. Gao, K. Davey, Y. Zheng, Y. Jiao and S. Z. Qiao, *Adv. Funct. Mater.*, 2023, **33**, 2300687.
13 M. Liu, W. Zou, J. Cong, N. Su, S. Qiu and L. Hou, *Small*, 2023, **19**, 2302698.
14 C. Lv, L. Zhong, H. Liu, Z. Fang, C. Yan, M. Chen, Y. Kong, C. Lee, D. Liu, S. Li, J. Liu, L. Song, G. Chen, Q. Yan and G. Yu, *Nat. Sustainability*, 2021, **4**, 868–876.
15 L. Chen, L. Wang, J. T. Ren, H. Y. Wang, W. W. Tian, M. L. Sun and Z. Y. Yuan, *Small Methods*, 2024, 2400108, DOI: **10.1002/smtd.202400108**.
16 Y. Zhu, C. Liu, S. Cui, Z. Lu, J. Ye, Y. Wen, W. Shi, X. Huang, L. Xue, J. Bian, Y. Li, Y. Xu and B. Zhang, *Adv. Mater.*, 2023, **35**, 2301549.
17 S. Zhou, H. He, J. Li, Z. Ye, Z. Liu, J. Shi, Y. Hu and W. Cai, *Adv. Funct. Mater.*, 2023, **34**, 2313770.
18 L. Wang, Y. Zhu, Y. Wen, S. Li, C. Cui, F. Ni, Y. Liu, H. Lin, Y. Li, H. Peng and B. Zhang, *Angew. Chem., Int. Ed.*, 2021, **60**, 10577–10582.
19 S. Zhou, S. Lv, J. Shi, L. Zhang, J. Li and W. Cai, *Chem. Eng. J.*, 2024, **484**, 149706.
20 Q. Zhang, Y. Hu, H. Wu, X. Zhao, M. Wang, S. Wang, R. Feng, Q. Chen, F. Song, M. Chen and P. Liu, *ACS Nano*, 2023, **17**, 1485–1494.
21 K. Shen, Y. Tang, Q. Zhou, Y. Zhang, W. Ge, X. Shai, S. Deng, P. Yang, S. Deng and J. Wang, *Chem. Eng. J.*, 2023, **471**, 144827.
22 Y. Li, H. Guo, J. Zhao, Y. Zhang, L. Zhao and R. Song, *Chem. Eng. J.*, 2023, **464**, 142604.
23 C. Kou, J. Zhou, H. Wang, J. Han, M. Han, A. Vomiero, Y. Liu and H. Liang, *Appl. Catal., B*, 2023, **330**, 122598.
24 P. Upale, S. Verma and S. B. Ogale, *J. Mater. Chem. A*, 2023, **11**, 8972–8987.
25 M.-L. Guo, Z.-Y. Wu, M.-M. Zhang, Z.-J. Huang, K.-X. Zhang, B.-R. Wang and J.-C. Tu, *Rare Met.*, 2023, **42**, 1847–1857.
26 M. Jiang, H. Zhai, L. Chen, L. Mei, P. Tan, K. Yang and J. Pan, *Adv. Funct. Mater.*, 2023, **33**, 2302621.
27 M. Cai, Q. Zhu, X. Wang, Z. Shao, L. Yao, H. Zeng, X. Wu, J. Chen, K. Huang and S. Feng, *Adv. Mater.*, 2022, **35**, 2209338.
28 D. Zhu, C. Guo, J. Liu, L. Wang, Y. Du and S.-Z. Qiao, *Chem. Commun.*, 2017, **53**, 10906–10909.
29 X. Gao, D. Chen, J. Qi, F. Li, Y. Song, W. Zhang and R. Cao, *Small*, 2019, **15**, e1904579.
30 J. Kim, M. C. Kim, S. S. Han and K. Cho, *Adv. Funct. Mater.*, 2024, **34**, 2315625.
31 K. Ge, S. Sun, Y. Zhao, K. Yang, S. Wang, Z. Zhang, J. Cao, Y. Yang, Y. Zhang, M. Pan and L. Zhu, *Angew. Chem., Int. Ed.*, 2021, **60**, 12097–12102.
32 X. Wang, Z. Li, S. Sun, H. Sun, C. Yang, Z. Cai, H. Zhang, M. Yue, M. Zhang, H. Wang, Y. Yao, Q. Liu, L. Li, W. Chu, J. Hu, X. Sun and B. Tang, *J. Colloid Interface Sci.*, 2024, **662**, 596–603.
33 H. Jin, X. Wang, C. Tang, A. Vasileff, L. Li, A. Slattery and S.-Z. Qiao, *Adv. Mater.*, 2021, **33**, 2007508.
34 X. Gao, D. Chen, J. Qi, F. Li, Y. Song, W. Zhang and R. Cao, *Small*, 2019, **15**, 1904579.
35 H. Qin, Y. Ye, J. Li, W. Jia, S. Zheng, X. Cao, G. Lin and L. Jiao, *Adv. Funct. Mater.*, 2022, **33**, 2209698.

